

1 **Weak stratospheric polar vortex events**
2 **modulated by the Arctic sea ice loss**

3
4 **Kazuhira Hoshi^{1*}, Jinro Ukita², Meiji Honda², Tetsu Nakamura³, Koji Yamazaki³,**
5 **Yasunobu Miyoshi⁴ and Ralf Jaiser⁵**

6
7 ¹Graduate School of Science and Technology, Niigata University, Niigata, Japan

8 ²Faculty of Science, Niigata University, Niigata, Japan

9 ³Faculty of Environmental Earth Science, Hokkaido University, Sapporo, Japan

10 ⁴Department of Earth and Planetary Sciences, Kyushu University, Fukuoka, Japan

11 ⁵Alfred-Wegener-Institute, Helmholtz-Zentrum für Polar-und Meeresforschung,
12 Potsdam, Germany

13
14 *Corresponding author: K. Hoshi (khoshi@env.sc.niigata-u.ac.jp)

15
16 **Key points:**

- 17 ● Sea-ice reduction in the Barents–Kara Sea (BKS) is a significant factor modulating
18 stratospheric weak polar vortex (WPV) events
- 19 ● Stationary Rossby wave response to BKS sea-ice loss enhances tropospheric
20 wavenumber-2 field, thus increasing upward wave propagation
- 21 ● WPV events in light-ice years tend to induce a stronger stratosphere–troposphere
22 coupling and Eurasian cold surface anomalies

23 **Abstract**

24

25 We characterize the differences in the upward planetary-scale wave propagation during
26 observed weak polar vortex (WPV) events between heavy- and light-sea-ice years in the
27 Barents–Kara Sea based on a composite analysis for the period of 1979–2015. Upward
28 wave propagation during WPV events in heavy-ice years is dominated by the
29 wavenumber-1 component. In contrast, WPV events occurring in light-ice years are
30 characterized by stronger wavenumber-2 propagation, which is caused by the
31 tropospheric wavenumber-2 response to sea-ice reduction in the Barents–Kara Sea.
32 Above observed features are supported by an Atmospheric General Circulation
33 Model experiment. Thus, under present climate conditions, Arctic sea-ice loss is a
34 possible factor modulating the wave propagation during the WPV events. We also find
35 that the WPV events in light-ice years have stronger stratosphere–troposphere coupling,
36 followed by colder mid-latitude surface conditions particularly over Eurasia.

37

38 **1 Introduction**

39 In the boreal winter stratosphere, a rapid weakening of the polar vortex over a
40 matter of several days can occur in association with a raise in stratospheric polar cap
41 temperature (Schoeberl, 1978; Limpasuvan et al., 2004). This event is known as sudden
42 stratospheric warming (SSW), which results from an enhanced upward propagation of
43 planetary-scale waves from the troposphere and the interaction of these planetary-scale
44 waves with the zonally averaged circulation (Charney & Drazin, 1961; Matsuno, 1971).
45 Because stratospheric signals may descend, leading to significant circulation anomalies
46 in the troposphere and associated weather and climate variations (Baldwin & Dunkerton,
47 2001; Polvani & Waugh, 2004), it is important to understand what factors control
48 upward propagation of planetary-scale waves, how these planetary waves interact with
49 the stratospheric polar vortex, and how anomalous stratospheric signals descend
50 downward to the troposphere.

51 Significant upward planetary wave propagation is composed mostly of zonal
52 wavenumber-1 (WN1) and wavenumber-2 (WN2) components, and the wave
53 propagation tends to occur in association with an emergence of tropospheric blocking
54 highs (Quiroz, 1986). Blocking highs over the Atlantic sector precede upward planetary
55 wave propagation from the WN1 component, and thus displacement-type SSWs tend to
56 occur, whereas blocking highs over western Europe or the eastern Pacific precede WN2
57 upward propagation and split-type SSWs (Martius et al., 2009; Castanheira &
58 Barriopedro, 2010; Nishii et al., 2011). Upward planetary wave propagation is also
59 modulated by El Niño-Southern Oscillation (ENSO). The significant WN1 upward

60 propagation and displacement-type SSW are frequently observed during El Niño
61 winters, whereas the WN2 upward propagation and split-type SSW are relatively
62 frequently observed during La Niña winters (Taguchi & Hartmann, 2006; Barriopedro
63 & Calvo, 2014; Song & Son, 2018). The quasi-biennial oscillation (QBO) is another
64 factor controlling the strength of the planetary wave propagation; thus more SSWs
65 occur during the easterly phase compared to the westerly phase (Labitzke, 1982).
66 Combined influences of ENSO and QBO on SSWs were also discussed based on
67 reanalysis data (Taguchi, 2015) and numerical simulation (Richter et al., 2011).

68 Several studies have reported that the recent significant Arctic sea-ice loss causes
69 a mean state response of enhanced upward wave propagation, weakened polar vortices,
70 and decreased mid-latitude surface temperatures due to the downward influence of
71 stratospheric signals (Cohen et al., 2014; García-Serrano et al., 2015; Nakamura et al.,
72 2015; Jaiser et al., 2016; King et al., 2016; Nakamura et al., 2016). The Barents–Kara
73 Sea (BKS) has also been identified as a key source region for the stationary Rossby
74 wave response resulting in a deepening of the climatological Siberian trough (Honda et
75 al., 2009) and for increased upward wave propagation (Kim et al., 2014, Sun et al.,
76 2015; Hoshi et al. 2017; Screen 2017; Zhang et al., 2017).

77 With this background we postulate that Arctic sea-ice anomalies in recent years
78 were another forcing factor for SSW events in addition to others such as ENSO and
79 QBO. However, directly testing such a conjecture based on reanalysis data is rather
80 difficult because of a small number of SSW events and the presence of its decadal
81 variability (e.g., Palmeiro et al., 2015). As a first step towards understanding of a

82 potential relationship between SSWs and sea ice variability, here we assess whether
83 sea-ice loss in the BKS modulates characteristics of weak polar vortex (WPV) events,
84 which are defined as those including not only SSWs but also events with less intense
85 polar vortex disturbances. In particular we examine how the BKS sea-ice loss
86 contributes to the modulation of each zonal wavenumber component in planetary-scale
87 and the spatial structures of significant upward wave propagation, based on a composite
88 analysis. We also support our findings with results from dedicated model experiments.

89

90 **2 Data and Methods**

91 We used the Japanese 55-year Reanalysis (JRA-55; Kobayashi et al., 2015), with
92 a 1.25° horizontal resolution and 37 vertical levels (1000–1 hPa) for atmospheric data,
93 and the Hadley Centre Sea Ice and Sea Surface Temperature data set version 2.2.0.0
94 (HadISST2; Titchner & Rayner, 2014) with a 1° spatial resolution and monthly mean
95 sea-ice concentration (SIC) data. Both datasets were analyzed in the period from
96 1979/80 to 2014/15, covering 36 boreal winter seasons. We computed the
97 two-dimensional Eliassen–Palm (E-P) flux (Andrews & McIntyre, 1976) and
98 three-dimensional wave–activity flux (Plumb, 1985) from 6-hourly data, and computed
99 the WN1 and WN2 components of the E-P flux from respective components of the
100 6-hourly atmospheric variables. All these 6-hourly data were converted to daily-mean
101 values. We then calculated the daily climatological values by applying a 31-day running
102 average to the 36-year averaged daily values, from which daily anomalies were
103 calculated as deviations.

104 We sampled WPV events occurring during the winter season (December to
105 February; DJF) because this is the season during which sea-ice anomalies enhance
106 upward planetary-scale wave propagation the most. To sample the WPV events, we
107 used the daily Northern Annular Mode (NAM; Thompson & Wallace, 2000) index,
108 which is the leading principal component time series of the 10 hPa geopotential height
109 northward 20°N during mid-winter (DJF) using the empirical orthogonal function (see
110 Butler et al., 2015, for a more detailed discussion on various criteria). Our criterion for
111 choosing WPV events was that the NAM index becomes less than -1σ . This date is
112 referred to as Day 0. After the polar vortex stabilized (the NAM index rose above $-$
113 1.0σ), we skipped three weeks to search for the next WPV event. This criterion allowed
114 us to sample 33 WPV events, including 21 SSW events. Note that here SSWs were
115 defined by a 10 hPa zonal mean zonal wind reversal at 60°N based on Charlton and
116 Polvani (2007), and SSW events which occurred within a 15-day difference from an
117 onset date of WPV events were counted. The gray bar graph in Figure 1a shows the
118 number of WPVs which occurred in each winter from 1979/80 to 2014/15, and the
119 black bars indicate the number of SSWs.

120 Next, we categorized those WPV events into heavy-ice WPVs or light-ice WPVs
121 based on the November–December mean SIC over the BKS (15°E–90°E, 70°N–85°N,
122 indicated by the green box in Figure 2a). Previous studies have reported that light-ice
123 conditions from late fall to early winter in the BKS are the most critical for the
124 enhancement of the mean state response of upward planetary wave propagation (e.g.,
125 King et al., 2016). When the SIC value exceeds plus or minus 0.5 standard deviation

126 during the 36-year period, we categorized the following winters into the heavy-ice and
127 light-ice winters, respectively. The time series and blue and red marks in Figure 1b
128 indicate the SIC index and heavy-ice and light-ice winters, respectively. The DJF mean
129 SIC anomalies averaged over the heavy-ice and light-ice winters which have WPVs are
130 shown in Figures 2a and 2b, respectively. After applying this sea-ice criterion to 33
131 initially sampled WPV events, we obtained 17 heavy-ice and 9 light-ice WPV events, of
132 which 9 and 7 were SSW events. We then carried out a composite analysis for both the
133 heavy-ice and light-ice WPV events centered at Day 0. In the following sections, we
134 will show composite averages of the anomalous fields. The statistical significance of the
135 composite anomalies was estimated using the two-sided Student's *t*-test with the null
136 hypothesis of no anomalies.

137 Due to an accelerated downward trend of SIC starting at around 2000–2005 (see
138 Figure 1b), the results of our composite analysis may not only reflect decadal scale
139 variability of WPVs/SSWs from sea ice changes, but also contain additional
140 compounded influences from increases in greenhouse gases. To reduce those possible
141 influences, we conducted two additional analyses. One approach used linearly
142 detrended data for both the SIC index and atmospheric variables. Another one was to
143 repeat the whole composite analysis based on a shorter time period (1979/80 to
144 2004/05), during which a linear trend in the BKS sea-ice time series was very weak or
145 almost absent. When we linearly detrend the BKS sea-ice time series, the heavy-ice
146 composite consists of winters in the middle period (i.e., the 1990s in which only a few
147 SSWs occurred), whereas the light-ice composite consists of winters mostly in early and

148 recent periods (i.e., the 1980s and years after 2005 in which SSWs frequently occurred).
149 Consequently, the simple detrending approach for the full period may emphasize the
150 decadal behavior of SSW events (Palmeiro et al., 2015). Since the shorter period does
151 not suffer from strong decadal behavior (Figure 1c), we will add our analysis on the
152 shorter period for checking the robustness of the results here and discuss the alternative
153 approach only briefly.

154

155 **3 Results**

156 **3.1 Wave–mean flow interaction**

157 Figure 3 shows the time evolutions of the zonal mean zonal wind anomaly at
158 60°N (top), the vertical E-P flux anomaly averaged over 40°N–80°N at 100 hPa
159 (middle), and the 2-m temperature anomaly averaged over the mid-latitude (50°N–
160 70°N) land region (bottom) for the heavy-ice and light-ice WPV composites. The 100
161 hPa level is used to represent the strength of upward planetary wave propagation (e.g.,
162 Polvani & Waugh, 2004). Both composites show weakened zonal mean zonal winds in
163 the upper stratosphere from around Day –5 and descending weakened zonal wind
164 signals (Figures 3a and 3b) in association with increased total E-P fluxes from Day –10
165 to Day +10 (indicated by black lines in Figures 3c and 3d). These results are consistent
166 with the general features of WPV and SSW events described in previous studies (e.g.,
167 Polvani & Waugh, 2004, Limpasuvan et al., 2004).

168 There are, however, marked differences between the two composites. The
169 stratospheric negative zonal wind anomaly and positive total E-P flux anomaly in the

170 light-ice composite are both larger than those in the heavy-ice composite. In the
171 wavenumber structure of the E-P flux anomalies, the WN1 component is dominated in
172 the heavy-ice composite from Day -10 to Day +5 (Figures 3c), whereas the light-ice
173 composite shows larger positive WN2 anomalies than the WN1 anomalies before Day 0
174 (Figure 3d). There are also marked differences in the troposphere after the onset of the
175 WPV events. The negative zonal wind signals in the stratosphere tend to connect with
176 those in the troposphere in the light-ice composite (Figure 3b), and surface temperature
177 over the mid-latitude land region decreases by 1–2 K (black line in Figure 3f). This
178 temperature decrease stands out in the Eurasian continent (0°E–180°E, indicated by
179 blue line).

180 Two factors may account for this stronger stratosphere–troposphere coupling in
181 light-ice WPV events. One is the strength of the sampled WPV events. The light-ice
182 composite has a higher rate of SSW events (7 out of 9) than the heavy-ice composite
183 does (9 out of 17); thus, the stratospheric influence is stronger. However, it is difficult
184 from observations to see if the higher rate results from lower sea-ice conditions or from
185 decadal variability of SSW events (e.g., winters in the 1980s and after 2000 had more
186 frequent SSW events than those in the 1990s, Palmeiro et al., 2015). Furthermore, the
187 rates of SSW to WPV depend on SSW definitions. If we define SSWs as a reversal of
188 10 hPa zonal wind averaged northward of 60°N (Butler et al., 2015), a difference of the
189 rates between the heavy-ice (14 out of 17) and light-ice (7 out of 9) winters becomes
190 smaller.

191 Another explanation for the stronger coupling is a modification of characteristics

192 of the polar vortex related to WN2-type features. Previous studies have pointed out that
193 split-type SSW events are related to WN2 anomalies and tend to have a stronger
194 downward influence than displacement-type SSW events do (Nakagawa & Yamazaki,
195 2006; Mitchell et al., 2013). Because the light-ice composite had a markedly stronger
196 WN2 E-P flux anomaly, this is also a potential mechanism of the stronger coupling.
197 Although clarifying the causes of the vertical coupling intensity is beyond our scope,
198 the obtained results suggest that WPV events occurring in light-ice years over the BKS
199 tend to strongly affect tropospheric circulation and mid-latitude surface temperature.
200 This is consistent with the results of Garfinkel et al. (2017) and Kretschmer et al. (2018)
201 showing that a recent low temperature anomaly in Eurasia was preceded by
202 stratospheric polar vortex weakening.

203

204 **3.2 Characteristics of upward planetary-scale wave propagation**

205 We next examine the mechanisms of upward planetary-scale wave propagation
206 and the three-dimensional geopotential height structure. Figure 4 shows the 10-day
207 (Day -10 to Day -1) mean field of the 250 hPa geopotential height anomalies, the
208 vertical structure of the eddy component (i.e., departure from the zonal mean) of the
209 geopotential height anomalies and the three-dimensional wave-activity flux anomalies
210 at 60°N for the heavy- and light-ice WPV composites. Note that upward wave-activity
211 flux anomalies reveal an enhanced upward wave propagation compared to the
212 climatological condition.

213 In the heavy-ice results, anticyclonic anomalies appear over Europe and Siberia,

214 and cyclonic anomalies appear over the Arctic and the Kamchatka Peninsula at the 250
215 hPa level (Figure 4a). The longitude-height cross-section (Figure 4c) shows that upward
216 wave-activity flux anomalies emanate from the two tropospheric precursors;
217 anticyclonic anomalies over Europe and the cyclonic anomalies over the Kamchatka
218 Peninsula. The position of the European anticyclonic anomaly is a precursory feature of
219 displacement-type SSW events reported by previous studies (Martius et al., 2009;
220 Castanheira & Barripedro, 2010; Nishii et al., 2011).

221 The 250 hPa geopotential height field of the light-ice WPV composite (Figure 4b)
222 is characterized by anticyclonic anomalies over the BKS and in a region extending
223 southward and by cyclonic anomalies from Siberia towards the North Pacific. These
224 anomalies show a wave pattern over Eurasia with a westward tilting geopotential height
225 structure (Figure 4d). The tilting is the strongest in the lower troposphere over the BKS.
226 In addition, positive turbulent heat flux anomalies are found in the BKS especially in
227 the previous 10 days (Day -20 to Day -11) (not shown). All these features are regarded
228 as manifestations of a vertically propagating stationary Rossby wave caused by sea-ice
229 reduction in the BKS as previously discussed (e.g., Honda et al., 2009; Hoshi et al.,
230 2017). Along with this upward propagating anomalous wave, upward and eastward
231 wave-activity flux anomalies are diagnosed from the lower troposphere to the upper
232 stratosphere. Another area of upward wave-activity fluxes is found around the
233 International Date Line, but these fluxes are not seen in the mid-to-upper stratosphere.
234 Thus, the WPVs in the light-ice winters tend to occur due to intensified upward
235 planetary-scale wave propagation by the stationary Rossby wave partly related to

236 sea-ice reduction in the BKS.

237 In the troposphere, the anticyclonic anomalies over the BKS seem to result from
238 a frequent occurrence of blocking highs, which precede split-type SSW events (e.g.,
239 Nishii et al., 2011). In the mid-to-upper stratosphere, the eddy geopotential height field
240 has a more complicated structure in light-ice conditions (Figures 4c and 4d), e.g. a
241 mixed signature from WN1 and WN2 geopotential height components. Those results
242 strongly support that the WPV events in light-ice years have WN2-type features.

243 We next decomposed the geopotential height field at 250 hPa into WN1 and WN2
244 components. Figure 5a shows the DJF winter-mean climatology. Figures 5b and 5c
245 show the composite anomalies (the deviation from the climatology) of the heavy-ice
246 and light-ice WPV events averaged from Day -10 to Day -1, respectively. In the
247 heavy-ice composite, the anomalous and climatological wave patterns appear to be
248 zonally in-phase only for the WN1 component. The maximum amplitude of the
249 anomalous WN1 pattern is 65 m at 59°N, which is much larger than that of the
250 anomalous WN2 field (37 m at 69°N). Note that the positive and negative regions of the
251 anomalous WN1 pattern around 60°N correspond to the two tropospheric precursors
252 identified in Figures 4a and 4c. From these facts, the heavy-ice composite is
253 characterized by the WN1 intensifications in the 250 hPa geopotential height field and
254 the 100 hPa E-P flux result (Figure 3c).

255 A contrasting picture emerges in the light-ice composite (Figure 5c). Both
256 anomalous WN1 and WN2 components of the 250 hPa geopotential fields are almost
257 zonally in-phase with the respective climatological wave fields. Moreover, both

258 components of the anomalous wave field are superposed constructively over the Eastern
259 Hemisphere. This is highly consistent with the wavy pattern in the Eurasian side in
260 Figure 4b. We deduce the following interpretation: the anomalous stationary Rossby
261 wave over Eurasia intensifies both the WN1 and WN2 components of the climatological
262 geopotential height field in the upper troposphere. As a consequence, both WN1 and
263 WN2 components of the vertical E-P flux are increased in the lower stratosphere
264 (Figure 3d). In contrast to the heavy-ice composite, we found that the maximum
265 amplitude of the anomalous WN2 component (66 m at 64°N) in the 250 hPa
266 geopotential height field is larger than that of the WN1 component (51 m at 78°N) with
267 a larger value of the WN2 E-P flux over the period of Day -10 to Day -1 (see Figure 3d).
268 This demonstrates the strengthened role of WN2 anomalies in the light ice composites.

269

270

271 **4 Discussions**

272 The results of our composite analysis may contain decadal time-scale variability
273 of WPVs/SSWs adding to our suggested influence from sea ice such as possible
274 compounded influences from increases in greenhouse gases. To reduce those influences,
275 we here show the results of the shorter period analysis for checking the robustness of
276 the results. The period we analyzed here is from 1979/80 to 2004/05, and the
277 composites are based on 9 heavy-ice and 6 light-ice events (Figure 1c). Note that,
278 although the sample size of those composites is smaller than that of our original
279 composites, this analysis possibly provides further information. We calculated

280 anomalies in this additional analysis as differences from the 31-day running averaged
281 daily climatological mean of the shorter period.

282 The results of E-P flux components show consistent characteristics related to the
283 results of the original composite; the larger WN2 component in the light-ice composite
284 (Figure 6d) and the dominant WN1 component in the heavy-ice composite (Figure 6c)
285 just before Day 0. A similar pattern to the original result is also found in 250 hPa
286 geopotential height anomalies averaged from Day -10 to Day -1; for example, an
287 amplified WN2 geopotential height field and the anomalous wave pattern over Eurasia
288 (not shown). Furthermore, a stronger stratosphere–troposphere coupling in the zonal
289 mean zonal wind field (Figure 6b) and negative surface air temperature anomalies in the
290 mid-latitude Eurasian regions (Figure 6f) were consistently found. The results for the
291 linear detrended analysis over the full 1979/80-2014/15 period are also consistent (not
292 shown). All these results imply that the characteristics obtained in our original analysis
293 (Figures 2-5) do not substantially depend on long-term climate change signals, but are
294 representing the features associated with the BKS sea ice loss. We note that in the
295 shorter-period light-ice composite mid-latitude cold anomalies are also seen before Day
296 0 (Figure 6f). We suggest that this is caused by the sea-ice influences via tropospheric
297 pathway, e.g. an intensification of the surface Siberian high (Honda et al., 2009; Mori et
298 al., 2014). However, the detailed mechanism and its relationship with WPVs are not a
299 main focus of this study.

300 We further evaluate the statistical significance for the WN2 contribution of the
301 original light-ice composite using the Monte Carlo Method. We examined the following

302 variables: the 100 hPa E-P flux anomaly and the amplitude of the raw (not the anomaly)
303 wave field in the 250 hPa geopotential height, both averaged 40°N–80°N and from Day
304 –10 to Day –1. The WN2 component of these two variables in the light-ice composite
305 are compared to 10,000 random subsamples of nine events taken from all 33 WPV
306 events. The null hypothesis is that the composite averaged value is not different from
307 the typical value of the WPVs. The p-values for the WN2 E-P flux anomaly and the
308 WN2 geopotential amplitude in the light-ice composite are 0.13 and 0.04, respectively.
309 These values provide supporting evidence for the notion that the light-ice composite has
310 a significantly different WN2 contribution especially in the geopotential height field
311 just before the onset of the WPV events compared with the average WPV condition.

312 The problem of small sample size in observations still remains. Thus, we also
313 analyzed a result of long-term integration using an Atmospheric General
314 Circulation Model (AGCM). The experiment we investigated here was conducted in
315 Nakamura et al. (2015), and also examined in Jaiser et al. (2016) and Hoshi et al. (2017).
316 We used the AGCM for the Earth Simulator (AFES; Ohfuchi et al., 2004) version 4.1,
317 model top of which is about 60 km, thus, it simulates the whole stratospheric circulation
318 as well as WPV events. We carefully treated sea ice in this model, and the simulated
319 turbulent heat flux in the Arctic is comparable with observations (see Nakamura et al.
320 (2015) for more details). We conducted two 60-year integrations after 11-year spin-up
321 under the same settings, except for Northern Hemisphere sea-ice conditions. One run
322 used the average annual cycle of the heavy-ice period (1979 to 1983; heavy-ice run),
323 and the other used the average annual cycle of the light-ice period (2005 to 2009;

324 light-ice run). The same average annual cycle of 1979 to 1983 was used for the SST
325 boundary condition. We note that these boundary conditions had the largest SIC
326 differences in the BKS in winter, and the simulated stratospheric circulation differences
327 mostly resulted from the BKS sea-ice reduction (Hoshi et al., 2017). Thus this AGCM
328 experiment is suitable for a comparison with the results from the reanalysis. To use
329 hindcast simulation results such as from the fifth Coupled Model Inter-comparison
330 Project may be another option. Although the analysis method would be comparable to
331 the reanalysis methods, the composite results also contain other effects indirectly in
332 addition to the sea ice. In our experiments, the simulated atmospheric differences come
333 only from the sea ice changes. Thus, we here adopted our simulation. We followed the
334 detection scheme of WPV events in the reanalysis data, except that the NAM index was
335 computed in the individual runs, and detected 62 and 56 WPV events in the heavy-ice
336 and light-ice runs, respectively (approximately one event per model year). Anomalies
337 were calculated as the differences from a 31-day running averaged climatology of the
338 heavy-ice experiment.

339 We plot histograms of E-P flux based on a larger number of WPV events from the
340 AFES experiments (Figure 7). The WN1 and WN2 components of vertical 100 hPa E-P
341 flux are averaged over 40 to 80°N over the period of Day -10 to Day 4 (15 days). We
342 here adopted the 15-day mean because in the light-ice experiment daily composite
343 values of the E-P fluxes peaked at around Day 0. However, features were similar if we
344 used 10-day average (Day -10 to Day -1). Focusing on peaks of the histograms of the
345 WN1 component, a negative shift was found in the light-ice experiment compared to the

346 heavy-ice experiment. In the WN2 component, the light-ice experiment shows a
347 positive shift, and WPVs which have a large WN2 contribution (e.g., larger than 35000
348 m^2s^{-2}) are more frequent in the light-ice experiment than in the heavy-ice experiment.
349 Computing the composite average of the WN2 E-P fluxes, the value of the light-ice
350 experiment is 10055 (m^2s^{-2}). This is 2.3 times larger than the value in the heavy-ice
351 experiment (4337 m^2s^{-2}), although these values are smaller than those in the reanalysis.
352 Statistical test showed that the composite anomalies (i.e., differences from the
353 climatology) of the WN2 component in each experiment are statistically significant at
354 the 99% confidence level, and the difference of the WN2 component between the
355 composites is also statistically significant at the 95% confidence level. In the composite
356 of geopotential height anomalies at 250 hPa averaged over 10-day period (Day -10 to
357 Day -1), a spatial pattern of the AGCM results highly resembles that of the reanalysis,
358 particularly wave pattern from the BKS region in the light-ice WPVs (not shown). The
359 above results provide supporting evidence for an active role of Arctic sea ice loss in
360 modulating WPV events, which is highly consistent when evaluating reanalysis data
361 and results from AGCM experiments.

362 There are a number of studies discussing factors that modulate wave propagation
363 during SSWs, e.g. ENSO and QBO (see Section 1). Thus, it should be clarified that the
364 Arctic sea-ice impacts pointed out here are independent of these factors. Using the
365 reanalysis data, we investigated whether the vertical WN2 E-P flux values of individual
366 WPV events in the original composites tend to be controlled by the specific ENSO or
367 QBO phases, and it suggested that those two factors were likely not a dominant

368 modulator (not shown). However, it is difficult to test this strictly from an inevitably
369 smaller subsamples of the short reanalysis time period. Our AFES simulation results
370 can deliver justification on this issue. Our model does not internally generate a QBO
371 (persistent weak easterlies in the equatorial zonal wind in the stratosphere, and a DJF
372 mean climatology at 50 hPa is -7.1 ms^{-1}), and the same annual cycle of SST was
373 prescribed as boundary condition for every model year in both experiments (DJF mean
374 monthly Niño 3.4 anomaly of 0.47 K, based on the data from National Oceanic and
375 Atmospheric Administration-Climate Prediction Center; NOAA-CPC). Although the
376 experiment is not perfect with regard to ENSO and QBO settings, simulated differences
377 come only from the sea-ice difference. Continuing, this suggests that the light-ice WPV
378 features, such as the WN2 E-P flux increase and the tropospheric precursory wave
379 pattern, were only modulated by the Arctic sea ice reduction.

380 We note that an amplitude of the WN2 E-P flux anomalies in the AFES
381 simulation was smaller than that in the reanalysis. One possible reason is that the
382 reanalysis results partly contain effects from QBO or ENSO indirectly. Additionally,
383 the results would contain internal variability, e.g., blocking high around the BKS and
384 the Ural region, which are the precursors of upward WN2 propagation. However, our
385 analysis cannot answer on this issue because the separation of those effects is difficult
386 due to the short observation record and small subsamples. Another possible reason of
387 the smaller WN2 amplitude may be the model biases. The climatological values of the
388 vertical WN2 E-P flux at 100 hPa are smaller in our model than those in the reanalysis,
389 thus a sensitivity of the WN2 would be also lower. This could be tested by analyzing

390 the simulation results using other AGCMs. However, this is not a main focus of this
391 study. We here emphasize that the light-ice WPV features are qualitatively highly
392 similar between the reanalysis and the AGCM simulation.

393 It has been discussed influences of blocking in the Ural region on the climate.
394 Chen et al. (2018) pointed out that quasi-stationary Ural Blocking contributes to a
395 reduction in the BKS sea ice. Our light-ice composite also has a feature resembling Ural
396 Blocking, e.g., anticyclonic anomalies around the BKS (see Figure 4b). However, sea
397 ice variability is very low and the lower sea-ice condition continues from Day -30 to
398 Day +30 (not shown). Thus in our light-ice composite, the anticyclonic anomalies over
399 the BKS are unlikely a cause of the sea ice reduction.

400

401 **5 Conclusions**

402 On the basis of the composite analysis applied to WPV events, we found distinct
403 characteristics in upward propagation of the planetary waves prior to the onset of the
404 WPVs depending on heavy- or light-sea-ice conditions. The heavy-ice composite is
405 characterized by a dominant WN1 contribution to the E-P flux increase (Figure 3c),
406 whereas the light-ice composite has a stronger WN2 contribution (Figure 3d). The
407 increased WN2 E-P flux is related to the amplified WN2 geopotential height field in the
408 upper troposphere (Figure 5c), which is due to the stationary Rossby wave propagation
409 over Eurasia (Figures 4b and 4d). The anomalous planetary wave field has the
410 characteristics of an atmospheric response pattern arising from sea-ice reduction in the
411 BKS (e.g., Honda et al., 2009; Hoshi et al., 2017). These results were supported by the

412 shorter-period analysis (Figure 6) and AGCM experiments (Figure 7). Thus, we
413 conclude that under present climate conditions Arctic sea-ice reduction also acts as an
414 important factor in modulating WPV properties in addition to ENSO and QBO.
415 Although our focus was on the WPV events, the fact that a significant portion of the
416 WPV events also includes SSWs (9 and 7 out of 17 and 9 heavy-ice and light-ice WPV
417 events, respectively). It is suggested that the obtained results can be partly extended to
418 SSW events.

419 Our results also indicate that light-ice WPV events feature a stronger
420 stratosphere–troposphere coupling in the zonal mean zonal wind field (Figures 3b and
421 6b) and an appearance of negative surface air temperature anomalies in mid-latitude
422 land regions particularly over Eurasia (Figures 3f and 6f) following to the onset of the
423 WPV events. This Eurasian surface temperature signals are also apparent in horizontal
424 maps averaged 30 days after Day 0 (Figures 8b and 8d). These results suggest that the
425 recent Eurasian cold conditions (Cohen et al., 2014; Garfinkel et al., 2017) were partly
426 related to stronger vertical coupling of the WPV events modulated by sea-ice loss. A
427 question remains about the mechanisms of the stronger vertical coupling. We pointed
428 out two possible causes in Section 3.1, namely, the stronger WPV events and the
429 WN2-type feature. Further examination is needed to clarify mechanisms of the different
430 vertical coupling strengths. Additionally, mechanisms of the different vertical coupling
431 intensity between displacement-type and split-type SSWs are still not clear. Further
432 investigation of the downward influences of SSWs will contribute to understanding the
433 coupling strength of light-ice WPV events.

434

435 **Acknowledgments**

436 We thank K. Nishii and P. J. Kushner for valuable discussions and comments. The
437 JRA-55 dataset was provided by the Japan Meteorological Agency
438 (<http://jra.kishou.go.jp/JRA-55/>). The HadISST2 data was downloaded from the Met
439 Office Hadley Centre website (<http://www.metoffice.gov.uk/hadobs/hadisst2/>), and
440 Nino 3.4 data was from the NOAA-CPC webpage
441 (http://origin.cpc.ncep.noaa.gov/products/analysis_monitoring/ensostuff/ONI_v5.php).

442 This study was in part supported by the Arctic Challenge for Sustainability (ArCS)
443 Project, the Belmont Forum InterDec Project, the Climate Initiative REKLIM, and
444 QUARCCS by the German Federal Ministry for Education and Research under grant
445 agreement 03F0777A. The authors acknowledge comments from two anonymous
446 reviewers which improve the manuscript.

447

448 **References**

- 449 Andrews, D. G., & McIntyre, M. E. (1976), Planetary waves in horizontal and vertical
450 shear: The generalized Eliassen-Palm relation and the mean zonal acceleration,
451 *Journal of the Atmospheric Sciences.*, 33(11), 2031–2048.
452 doi:10.1175/1520-0469(1976)033<2031:PWIHAV>2.0.CO;2
- 453 Baldwin, M. P., & Dunkerton, T. J. (2001), Stratospheric harbingers of anomalous
454 weather regimes, *Science*, 294(5542), 581–584. doi:10.1126/science.1063315
- 455 Barriopedro, D., & Calvo, N. (2014), On the Relationship between ENSO, Stratospheric
456 Sudden Warmings, and Blocking, *Journal of Climate*, 27(12), 4704–4720.
457 Doi:10.1175/JCLI-D-13-00770.1
- 458 Butler, A.H., Seidel, D.J., Hardiman, S.C., Butchart, N., Birner, T., & Match, A. (2015),
459 Defining Sudden Stratospheric Warmings, *Bulletin of the American Meteorological*
460 *Society*, 96, 1913–1928. doi:10.1175/BAMS-D-13-00173.1
- 461 Castanheira, J. M., & Barriopedro, D. (2010), Dynamical connection between
462 tropospheric blockings and stratospheric polar vortex. *Geophysical Research Letters*,
463 37(13), L13809. doi:10.1029/2010GL043819
- 464 Charlton, A. J., & Polvani, L. M. (2007), A new look at stratospheric sudden warmings.
465 Part I: Climatology and modeling benchmarks, *Journal of Climate*, 20(3), 449–469.
466 Doi:10.1175/JCLI3996.1
- 467 Charney, J. G., & Drazin, P. G. (1961), Propagation of planetary - scale disturbances
468 from the lower into the upper atmosphere, *Journal of Geophysical Research*, 66(1),
469 83-109. doi:10.1029/JZ066i001p00083

470 Chen, X., Luo, D., Feldstein, S. B., & Lee, S. (2018), Impact of winter Ural blocking on
471 Arctic sea ice: short-time variability, *Journal of Climate*, 31(6), 2267-2282. doi:
472 10.1175/JCLI-D-17-0194.1

473 Cohen, J., Screen, J. A., Furtado, J. C., Barlow, M., Whittleston, D., Coumou, D., &
474 Jones, J. (2014), Recent Arctic amplification and extreme mid-latitude weather,
475 *Nature geoscience*, 7(9), 627–637. doi:10.1038/ngeo2234

476 García-Serrano, J., Frankignoul, C., Gastineau, G., & de la Cámara, A. (2015), On the
477 predictability of the winter Euro-Atlantic climate: Lagged influence of autumn Arctic
478 sea ice, *Journal of Climate*, 28(13), 5195–5216. doi:10.1175/JCLI-D-14-00472.1

479 Garfinkel, C. I., Son, S.-W., Song, K., Aquila, V., & Oman, L. D. (2017), Stratospheric
480 variability contributed to and sustained the recent hiatus in Eurasian winter warming,
481 *Geophysical Research Letters*, 44(1), 374–382. doi:10.1002/2016GL072035

482 Honda, M., Inoue, J., & Yamane, S. (2009), Influence of low Arctic sea-ice minima on
483 anomalously cold Eurasian winters, *Geophysical Research Letters*, 36(8), L08707.
484 doi:10.1029/2008GL037079

485 Hoshi, K., Ukita, J., Honda, M., Iwamoto, K., Nakamura, T., Yamazaki, K., Dethloff,
486 K., Jaiser, R., & Handorf, D. (2017), Poleward eddy heat flux anomalies associated
487 with recent Arctic sea ice loss, *Geophysical Research Letters*, 44(1), 446–454.
488 doi:10.1002/2016GL071893

489 Jaiser, R., Nakamura, T., Handorf, D., Dethloff, K., Ukita, J., & Yamazaki, K. (2016),
490 Atmospheric autumn and winter response to Arctic sea ice changes in reanalysis data
491 and model simulations, *Journal of Geophysical Research: Atmospheres*, 121(13),

492 7564–7577. doi:10.1002/2015JD024679

493 Kim, B.-M., Son, S.-W., Min, S.-K., Jeong, J.-H., Kim, S.-J., Zhang, X., Shim, T., &
494 Yoon, H.-J. (2014), Weakening of the stratospheric polar vortex by Arctic sea-ice
495 loss, *Nature communications*, 5, 4646. doi:10.1038/ncomms5646

496 King, P., M., Hell, M., & Keenlyside, N. (2016), Investigation of the atmospheric
497 mechanisms related to the autumn sea ice and winter circulation link in the Northern
498 Hemisphere, *Climate dynamics*, 46(3-4), 1185. doi:10.1007/s00382-015-2639-5

499 Kobayashi, S., Ota, Y., Harada, Y., Ebata, A., Moriyama, M., Onoda, H., Onogi, K.,
500 Kamahori, H., Kobayashi, C., Endo, H., Miyaoka, K., & Takahashi, K. (2015), The
501 JRA-55 Reanalysis: general specifications and basic characteristics, *Journal of the*
502 *Meteorological Society of Japan. Ser. II.*, 93(1), 5–48. doi:10.2151/jmsj.2015-001

503 Kretschmer, M., Coumou, D., Agel, L., Barlow, M., Tziperman, E., and Cohen, J.
504 (2018), More-Persistent Weak Stratospheric Polar Vortex States Linked to Cold
505 Extremes, *Bull. Amer. Meteor. Soc.*, 99, 49-60. doi:10.1175/BAMS-D-16-0259.1.

506 Labitzke, K. (1982), On the interannual variability of the middle stratosphere during the
507 northern winters, *Journal of the Meteorological Society of Japan. Ser. II.*, 60(1),
508 124–139. doi:10.2151/jmsj1965.60.1_124

509 Limpasuvan, V., Thompson, D. W. J., & Hartmann, D. L. (2004), The life cycle of the
510 Northern Hemisphere sudden stratospheric warmings, *Journal of Climate*, 17(13),
511 2584–2596. doi:10.1175/1520-0442(2004)017<2584:TLCOTN>2.0.CO;2

512 Martius, O., Polvani, L. M., & Davies, H. C. (2009), Blocking precursors to
513 stratospheric sudden warming events, *Geophysical Research Letters*, 36(14), L14806.

514 doi:10.1029/2009GL038776

515 Matsuno, T. (1971), A dynamical model of the stratospheric sudden warming, *Journal*
516 *of the Atmospheric Sciences*, 28(8), 1479–1494.
517 doi:10.1175/1520-0469(1971)028<1479:ADMOTS>2.0.CO;2

518 Mitchell, D. M., Gray, L. J., Anstey, J., Baldwin, M. P., & Charlton-Perez, A. J. (2013),
519 The influence of stratospheric vortex displacements and splits on surface climate,
520 *Journal of Climate*, 26(8), 2668–2682. doi:10.1175/JCLI-D-12-00030.1

521 Mori, M., Watanabe, M., Shiogama, H., Inoue, J., & Kimoto, M. (2014). Robust Arctic
522 sea-ice influence on the frequent Eurasian cold winters in past decades, *Nature*
523 *Geoscience*, 7(12), 869, [doi:10.1038/ngeo2277](https://doi.org/10.1038/ngeo2277)

524 Nakagawa, K. I., & Yamazaki, K. (2006), What kind of stratospheric sudden warming
525 propagates to the troposphere?, *Geophysical Research Letters*, 33(4), L04801.
526 doi:10.1029/2005GL024784

527 Nakamura, T., Yamazaki, K., Iwamoto, K., Honda, M., Miyoshi, Y., Ogawa, Y., &
528 Ukita, J. (2015), A negative phase shift of the winter AO/NAO due to the recent
529 Arctic sea-ice reduction in late autumn, *Journal of Geophysical Research:*
530 *Atmospheres*, 120(8), 3209–3227. doi:10.1002/2014JD022848

531 Nakamura, T., Yamazaki, K., Iwamoto, K., Honda, M., Miyoshi, Y., Ogawa, Y.,
532 Tomikawa, Y., & Ukita, J. (2016), The stratospheric pathway for Arctic impacts on
533 midlatitude climate, *Geophysical Research Letters*, 43(7), 3494–3501.
534 doi:10.1002/2016GL068330

535 Nishii, K., Nakamura, H., & Orsolini, Y. J. (2011), Geographical dependence observed

536 in blocking high influence on the stratospheric variability through enhancement and
537 suppression of upward planetary-wave propagation, *Journal of Climate*, 24(24),
538 6408–6423. doi:10.1175/JCLI-D-10-05021.1

539 Palmeiro, F. M., Barriopedro, D., García-Herrera, R., & Calvo, N. (2015), Comparing
540 Sudden Stratospheric Warming Definitions in Reanalysis Data, *Journal of Climate*,
541 28(17), 6823–6840. doi:10.1175/JCLI-D-15-0004.1

542 Plumb, R. A. (1985), On the three-dimensional propagation of stationary waves,
543 *Journal of the Atmospheric Sciences*, 42(3), 217–229.
544 doi:10.1175/1520-0469(1985)042<0217:OTTDPO>2.0.CO;2

545 Polvani, L. M., & Waugh, D. W. (2004), Upward wave activity flux as a precursor to
546 extreme stratospheric events and subsequent anomalous surface weather regimes.,
547 *Journal of Climate*, 17(18), 3548–3554.
548 doi:10.1175/1520-0442(2004)017<3548:UWAFAA>2.0.CO;2

549 Quiroz, R. S. (1986), The association of stratospheric warmings with tropospheric
550 blocking, *Journal of Geophysical Research: Atmospheres*, 91(D4), 5277–5285.
551 doi:10.1029/JD091iD04p05277

552 Richter, J. H., Matthes, K., Calvo, N., and Gray, L. J. (2011), Influence of the quasi -
553 biennial oscillation and El Niño-Southern Oscillation on the frequency of sudden
554 stratospheric warmings, *J. Geophys. Res.*, 116, D20111. doi:10.1029/2011JD015757

555 Schoeberl, M. R. (1978), Stratospheric warmings: Observations and theory, *Rev*
556 *Geophys*, 16(4), 521–538. doi:10.1029/RG016i004p00521

557 Screen, J. A. (2017), Simulated Atmospheric Response to Regional and Pan-Arctic Sea

558 Ice Loss, *Journal of Climate*, 30(11), 3945-3962. doi:10.1175/JCLI-D-16-0197.1

559 Song, K. and Son, S.-W., (2018), Revising the ENSO-SSW relationship, *Journal of*
560 *Climate*, 31, 2133-2143

561 Sun, L., C. Deser, & Tomas, R. A. (2015), Mechanisms of stratospheric and
562 tropospheric circulation response to projected Arctic sea ice loss, *Journal of Climate*,
563 28(19), 7824–7845. doi:10.1175/JCLI-D-15-0169.1

564 Taguchi, M., & Hartmann, D. L. (2006), Increased occurrence of stratospheric sudden
565 warmings during El Niño as simulated by WACCM, *Journal of Climate*, 19(3), 324–
566 332. doi:10.1175/JCLI3655.1

567 Taguchi, M. (2015), Changes in frequency of major stratospheric sudden warmings with
568 El Niño/Southern Oscillation and quasi-biennial oscillation: *J. Meteor. Soc. Japan*,
569 93, 99-115

570 Thompson, D. W. J., & Wallace, J. M. (2000), Annular modes in the extratropical
571 circulation: Part I. Month to month variability, *Journal of Climate*, 13(5),1000–1016.
572 doi:10.1175/1520-0442(2000)013<1000:AMITEC>2.0.CO;2

573 Titchner, H. A., & Rayner, N. A. (2014), The Met Office Hadley Centre sea ice and sea
574 surface temperature data set, version 2: 1. Sea ice concentrations, *Journal of*
575 *Geophysical Research. Atmospheres*, 119(6), 2864–2889.
576 doi:10.1002/2013JD020316

577 Zhang, P., Wu, Y., & Smith, K. L. (2017), Prolonged effect of the stratospheric pathway
578 in linking Barents–Kara Sea ice variability to the midlatitude circulation in a
579 simplified model, *Climate Dynamics*, 1–13. doi:10.1007/s00382-017-3624-y

580

581

582 Figures

583

584 **Figure 1.** (a) The number of weak polar vortex (WPV) events that occurred in each
585 winter from 1979/80 to 2014/15 (gray bars) based on the JRA-55 data. The black bars
586 indicate the number of sudden stratospheric warming (SSW) events. Time series of
587 November–December mean sea-ice concentration (SIC; %) averaged over the Barents–
588 Kara Sea (BKS; 15°E–90°E, 70°N–85°N) in the period of (b) 1979/80–2014/15 and (c)
589 1979/80–2004/05, based on the HadISST2 data. The SIC values that exceed plus
590 (minus) 0.5 standard deviation during respective periods are marked by blue (red)
591 circles.

592

593 **Figure 2.** Composite anomalies of the December–February (DJF) mean SIC (%) for the
594 (a) heavy-ice and (b) light-ice winters. The anomaly is a deviation from the DJF
595 climatological mean. Green box in Figure 2a represents the BKS region used for the
596 SIC index. The HadISST2 data was used.

597

598 **Figure 3.** Composite anomalies of (top panels) the time-height cross-section of zonal
599 mean zonal wind at 60°N (contour; m s^{-1}), (middle panels) 40°N–80°N averaged
600 vertical Eliassen-Palm (E-P) flux anomalies at 100 hPa ($10^4 \text{ m}^{-2} \text{ s}^{-2}$), and (bottom
601 panels) 50°N–70°N land averaged 2-m temperature anomaly (K), for (left) heavy-ice
602 and (right) light-ice WPV events, based on the JRA-55 data. The black, green, and
603 purple lines in the middle panels indicate the total, zonal wavenumber-1 (WN1), and

604 zonal wavenumber-2 (WN2) components of the E-P flux anomalies, respectively. The
605 black and blue lines in the bottom panels indicate the zonally and Eurasian continent
606 (0°E - 180°E) averaged values, respectively. Shading in the top panels and the circle in
607 the middle and bottom panels indicate statistical significance at the 90% level.

608

609 **Figure 4.** Composite anomalies in geopotential height at 250 hPa (shade; m) averaged
610 from Day -10 to Day -1 for (a) heavy-ice and (b) light-ice WPV events, based on the
611 JRA-55 data. Solid and dashed lines indicate statistical significance at the 90% and 95%
612 levels, respectively. Longitude-height cross-section of the eddy component of
613 geopotential height anomalies (contours) at 60°N averaged from Day -10 to Day -1 for
614 (c) heavy-ice and (d) the light-ice WPV composites. The contour interval is 20 m, and 0
615 m is omitted. Shading indicates statistical significance at the 95% level. Arrows indicate
616 the anomalies of the zonal and vertical components of the wave-activity flux ($\text{m}^2 \text{s}^{-2}$)
617 defined by Plumb (1985). Anomalous vectors with small positive or negative vertical
618 values (smaller than 0.005) are not plotted, and the vectors are scaled by the reciprocal
619 square root of the density.

620

621 **Figure 5.** WN1 (contours) and WN2 (shade) components of the 250 hPa geopotential
622 height (m) for (a) December-February (DJF) mean climatology (1979/80 to 2014/15)
623 and composite anomalies averaged from Day -10 to Day -1 for (b) heavy-ice and (c)
624 light-ice WPV events. The JRA-55 data was used.

625

626 **Figure 6.** Same as Figure 3, but the results of the shorter period analysis from 1979/80
627 to 2004/05. Anomalies represent differences from climatological mean of the shorter
628 period.

629

630 **Figure 7.** Histograms of 100 hPa E-P flux anomalies averaged over 40–80°N and
631 15-day mean (from Day -10 to 4), for the WPV events from the heavy-ice
632 (blue) and light-ice (orange) AFES experiments. Upper and Lower panels
633 show the results of WN1 and WN2 components, respectively.

634

635 **Figure 8.** Composite anomalies in 2m temperature (shade; m) averaged over the period
636 from Day 0 to Day 29 (30 days) for (left) heavy-ice and (right) light-ice WPV events,
637 based on the JRA-55 data. Upper and lower panels are the results of the original and
638 shorter-period analyses. Solid line indicates statistical significance at the 95% level.

639

640

641

642

643 Figures

644

645

646

647

648

649

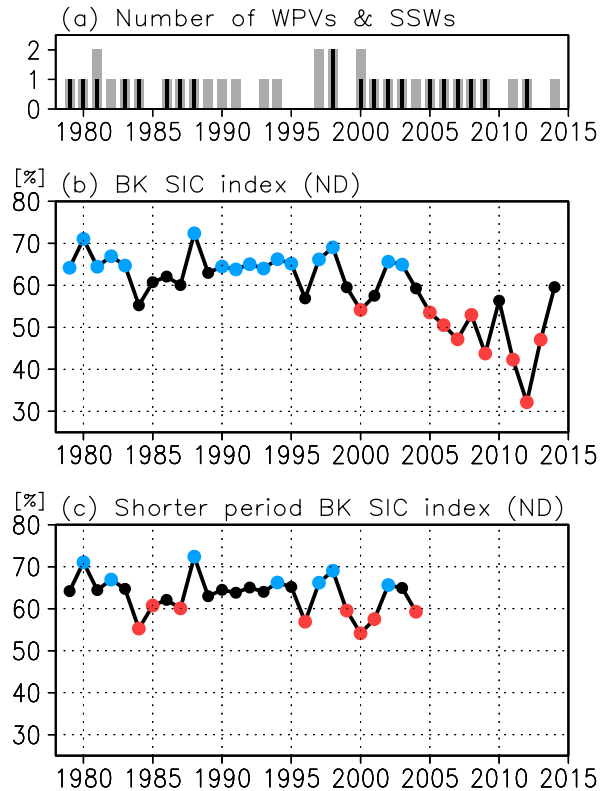
650

651

652

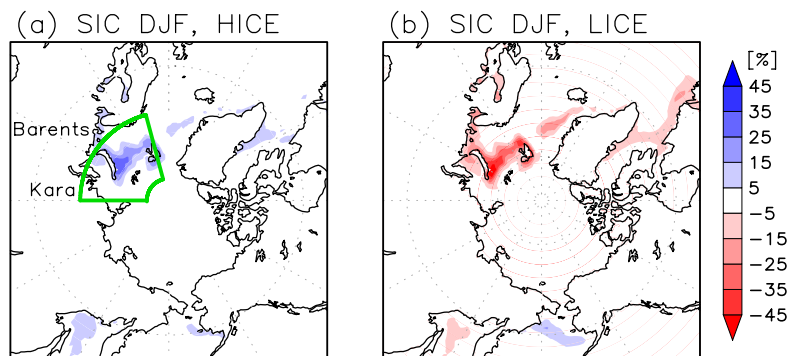
653

654



655 **Figure 1.** (a) The number of weak polar vortex (WPV) events that occurred in each
656 winter from 1979/80 to 2014/15 (gray bars) based on the JRA-55 data. The black bars
657 indicate the number of sudden stratospheric warming (SSW) events. Time series of
658 November–December mean sea-ice concentration (SIC; %) averaged over the Barents–
659 Kara Sea (BKS; 15°E–90°E, 70°N–85°N) in the period of (b) 1979/80–2014/15 and (c)
660 1979/80–2004/05, based on the HadISST2 data. The SIC values that exceed plus
661 (minus) 0.5 standard deviation during respective periods are marked by blue (red)
662 circles.

663



664

665 **Figure 2.** Composite anomalies of the December–February (DJF) mean SIC (%) for the
 666 (a) heavy-ice and (b) light-ice winters. The anomaly is a deviation from the DJF
 667 climatological mean. Green box in Figure 2a represents the BKS region used for the
 668 SIC index. The HadISST2 data was used.

669

670

671

672

673

674

675

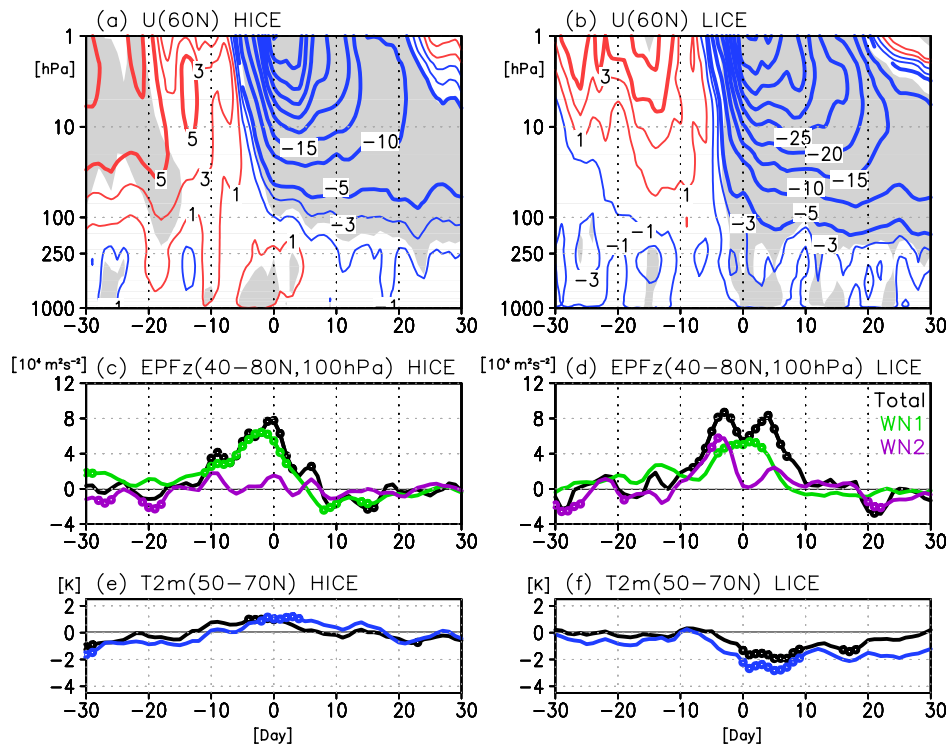
676

677

678

679

680



681 **Figure 3.** Composite anomalies of (top panels) the time-height cross-section of zonal

682 mean zonal wind at 60°N (contour; m s⁻¹), (middle panels) 40°N–80°N averaged

683 vertical Eliassen-Palm (E-P) flux anomalies at 100 hPa (10⁴ m² s⁻²), and (bottom

684 panels) 50°N–70°N land averaged 2-m temperature anomaly (K), for (left) heavy-ice

685 and (right) light-ice WPV events, based on the JRA-55 data. The black, green, and

686 purple lines in the middle panels indicate the total, zonal wavenumber-1 (WN1), and

687 zonal wavenumber-2 (WN2) components of the E-P flux anomalies, respectively. The

688 black and blue lines in the bottom panels indicate the zonally and Eurasian continent

689 (0°E–180°E) averaged values, respectively. Shading in the top panels and the circle in

690 the middle and bottom panels indicate statistical significance at the 90% level.

691

692

693

694

695

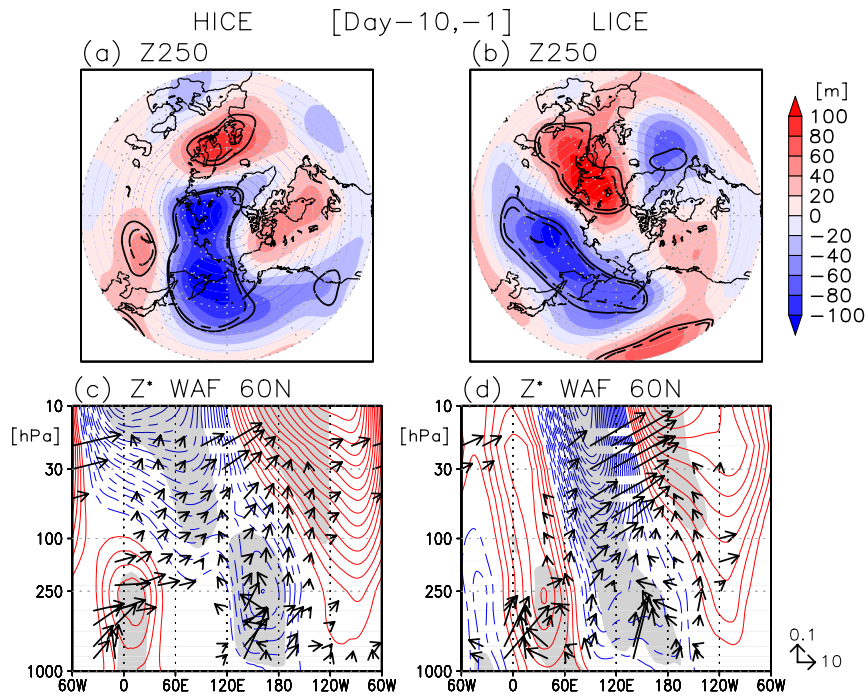
696

697

698

699

700



701 **Figure 4.** Composite anomalies in geopotential height at 250 hPa (shade; m) averaged

702 from Day -10 to Day -1 for (a) heavy-ice and (b) light-ice WPV events, based on the

703 JRA-55 data. Solid and dashed lines indicate statistical significance at the 90% and 95%

704 levels, respectively. Longitude-height cross-section of the eddy component of

705 geopotential height anomalies (contours) at 60°N averaged from Day -10 to Day -1 for

706 (c) heavy-ice and (d) the light-ice WPV composites. The contour interval is 20 m, and 0

707 m is omitted. Shading indicates statistical significance at the 95% level. Arrows indicate

708 the anomalies of the zonal and vertical components of the wave-activity flux ($\text{m}^2 \text{s}^{-2}$)

709 defined by Plumb (1985). Anomalous vectors with small positive or negative vertical

710 values (smaller than 0.005) are not plotted, and the vectors are scaled by the reciprocal

711 square root of the density.

712

713

714

715

716

717

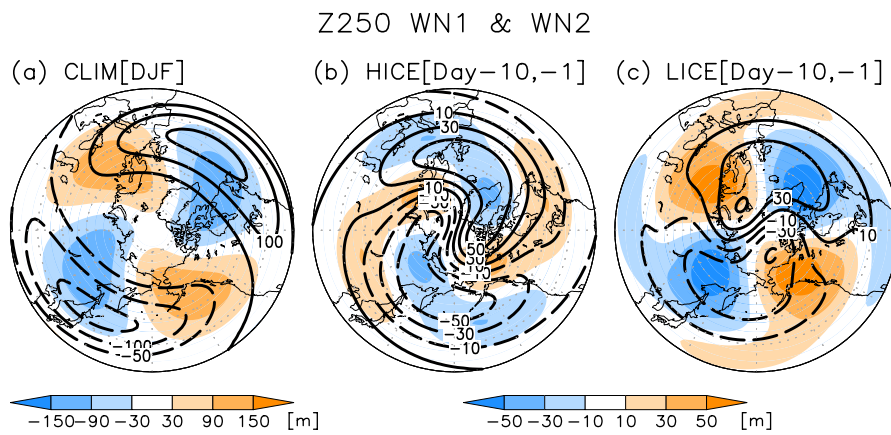
718

719

720

721 **Figure 5.** WN1 (contours) and WN2 (shade) components of the 250 hPa geopotential
722 height (m) for (a) December–February (DJF) mean climatology (1979/80 to 2014/15)
723 and composite anomalies averaged from Day –10 to Day –1 for (b) heavy-ice and (c)
724 light-ice WPV events. The JRA-55 data was used.

725



726

727

728

729

730

731

732

733

734

735

736

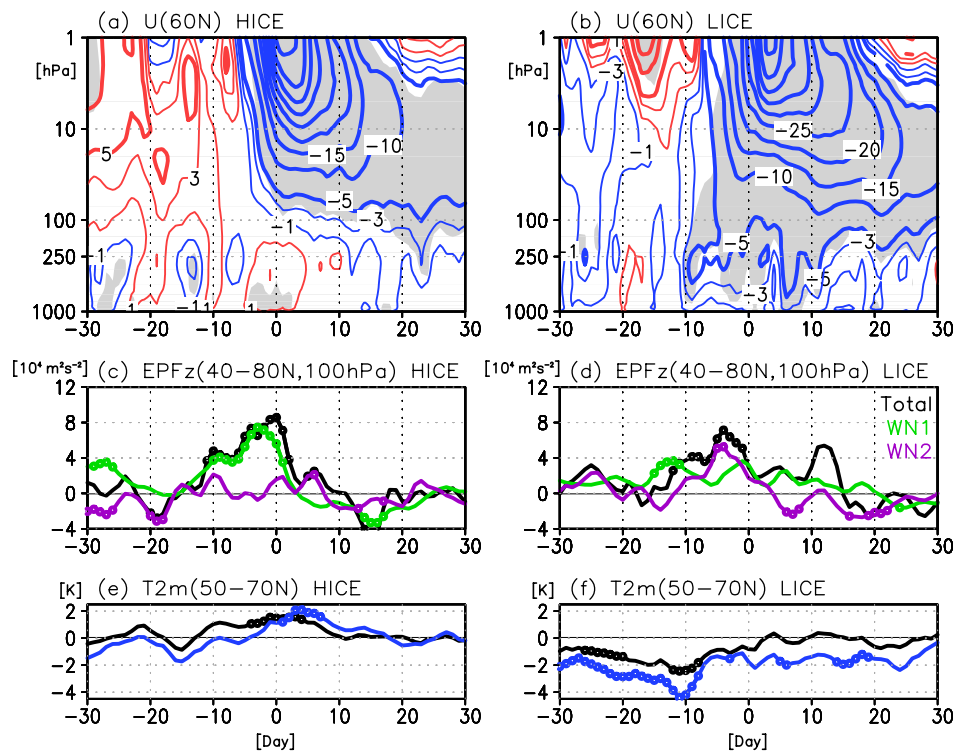
737

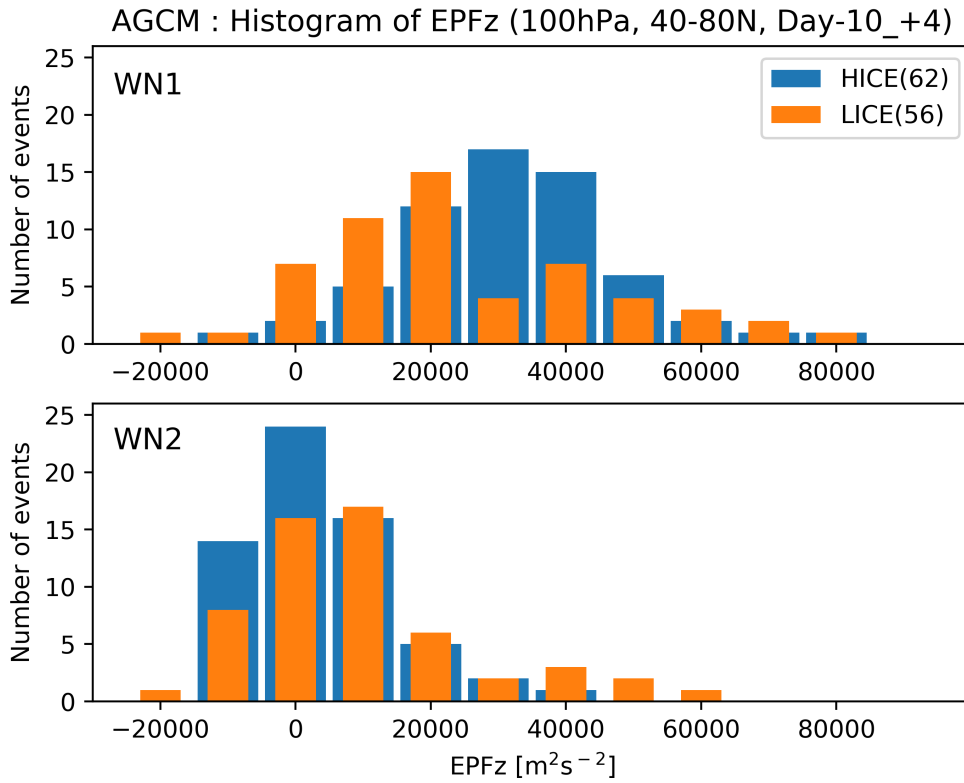
738 **Figure 6.** Same as Figure 3, but the results of the shorter period analysis from 1979/80

739 to 2004/05. Anomalies represent differences from climatological mean of the shorter

740 period.

741





742

743 **Figure 7.** Histograms of 100 hPa E-P flux anomalies averaged over 40–80°N and

744 15-day mean (from Day -10 to 4), for the WPV events from the heavy-ice

745 (blue) and light-ice (orange) AFES experiments. Upper and Lower panels

746 show the results of WN1 and WN2 components, respectively.

747

748

749

750

751

752

753

754

755

756

757

758

759

760

761

762

763

764

765

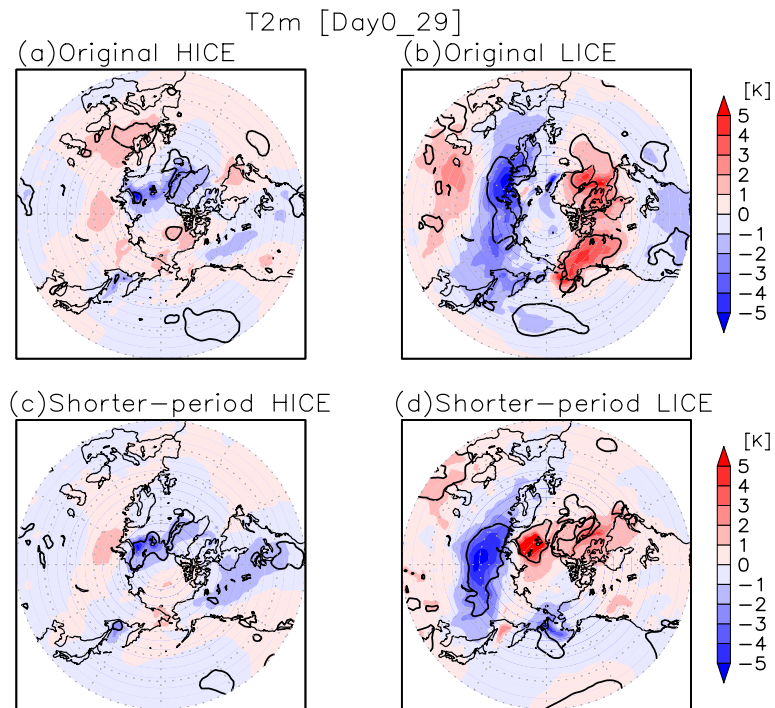


Figure 8. Composite anomalies in 2m temperature (shade; m) averaged over the period from Day 0 to Day 29 (30 days) for (left) heavy-ice and (right) light-ice WPV events, based on the JRA-55 data. Upper and lower panels are the results of the original and shorter-period analyses. Solid line indicates statistical significance at the 95% level.